Oil Shale, 2026, 43, 2, 197–227 https://doi.org/10.3176/oil.2026.2.04

Numerical investigation of superheated steam injection for in situ oil shale exploitation: fracture network optimization and energy efficiency analysis

Jianzheng Su[a,b], Dong Yang[c,d], Xudong Huang[c,d]*

[a] State Center for Research and Development of Oil Shale Exploitation, 31 Xueyuan Road, Haidian District, Beijing 100083, China
[b] Sinopec Petroleum Exploration and Production Research Institute, 31 Xueyuan Road, Haidian District, Beijing 100083, China
[c] Key Lab of In situ Property-improving Mining of Ministry of Education, Taiyuan University of Technology, 79 West Yingze Street, Wanbailin District, Taiyuan, Shanxi Province 030024, China
[d] In situ Steam Injection Branch of State Center for Research and Development of Oil Shale Exploitation, Taiyuan University of Technology, 79 West Yingze Street, Wanbailin District, Taiyuan, Shanxi Province 030024, China

Received 18 July 2025, accepted 8 April 2026, available online 16 April 2026

Abstract. *This study numerically investigates in situ oil shale exploitation by superheated steam injection, emphasizing coupled thermo-hydraulic-mechanical processes. An anisotropic multi-field model was developed to evaluate how hydraulic fracture distribution and thermally activated weak planes affect oil/gas recovery and energy return. Using conditions from the Balikun deposit (Xinjiang), four cases were simulated (1–2 hydraulic fractures, with/without weak-plane evolution). Weak-plane activation markedly improves heating via alternating convection and conduction, expanding high-temperature zones and achieving 90.5% oil recovery after 1000 days. Without it, heating is limited (< 60% recovery) and production declines rapidly. Energy return rates peak early (5.79–8.44) but decay without fracture evolution, whereas activated weak planes sustain values > 5 for over a year. Doubling initial fractures boosts recovery by 46% but only slightly improves energy efficiency due to higher steam consumption.*

Keywords: *oil shale, numerical simulation, superheated steam, energy return rate, fracture network.*

* Corresponding author, huangxudong@tyut.edu.cn

1. Introduction

Oil shale, a sedimentary rock rich in immature organic matter, serves as a critical supplementary energy resource to conventional fossil fuels due to its vast global reserves [1, 2]. Under high-temperature conditions, the organic kerogen within oil shale undergoes pyrolysis to produce shale oil and gas. However, conventional mining methods (e.g., underground or open-pit mining) are economically unfeasible for deeply buried oil shale deposits due to low energy density and high extraction costs [3]. Consequently, in situ exploitation has emerged as a promising strategy for mid-to-deep oil shale development. Among existing techniques, the MTI (Mining Technology Institute) method, pioneered by Zhao et al. [4], employs superheated steam as a heat carrier to thermally decompose kerogen while simultaneously transporting pyrolyzed products to the ground. This method involves three key steps: (1) drilling wells in target areas, (2) hydraulic fracturing to establish interconnected fracture networks as initial steam channels, and (3) injecting superheated steam to initiate and sustain pyrolysis.

The in situ steam injection process involves complex thermo-hydro-mechanical-chemical (THMC) coupling effects. Steam injection alters the permeability and mechanical properties of oil shale through thermal expansion, pore pressure changes, and anisotropic deformation [5]. These dynamic interactions, in turn, influence steam flow, heat transfer efficiency, and hydrocarbon recovery rates, ultimately determining the economic viability of the process. While laboratory experiments have provided valuable insights into temperature-dependent properties such as density [6 , 7], permeability [8, 9], and thermal conductivity [9–11], replicating in situ multi-field coupling conditions remains challenging. Field trials, though critical, are cost-prohibitive and lack repeatability, underscoring the need for cost-effective numerical simulations to bridge this gap [13, 14].

Prior studies have focused predominantly on temporal-spatial variations in temperature, seepage, and stress fields during in situ heating. For instance, Kang et al. [14] developed a coupled thermo-hydraulic-mechanical (THM) model to analyze anisotropic heat transfer and deformation in oil shale. Wang et al. [15] further incorporated temperature-dependent anisotropy in thermal conductivity and permeability, revealing how directional heterogeneity affects heating efficiency. Recent advancements include comparative analyses of heating methods (e.g., electromagnetic, microwave, and steam injection) [16–18] and sustainable energy integration [19]. However, existing research largely neglects critical economic metrics such as energy return rate (ERR) and hydrocarbon recovery efficiency, limiting their practical relevance [20–22].

To address this gap, this study integrates temperature-dependent porosity, fracture connectivity, and anisotropic permeability into a THM-coupled numerical model. Using the geological conditions of Xinjiang's Balikun oil shale deposit as a reference, we investigate how hydraulic fracture

configurations and thermally activated weak planes influence hydrocarbon recovery, ERR, and operational longevity. By coupling experimental data with multi-physics simulations, this work provides actionable strategies for optimizing in situ oil shale exploitation, balancing technical performance with economic feasibility.

2. Establishment of THM coupling mathematical model and determination of initial/boundary conditions

2.1. Fundamental assumptions

In situ steam injection for oil shale extraction involves complex physico-chemical processes. To balance computational tractability while preserving the essential physics of in situ thermal recovery, the following simplifying assumptions are adopted:

(1) Continuum medium approximation: The oil shale formation and its overburden/underburden strata are treated as statistically homogeneous continua at the engineering scale. Macroscopic physical-mechanical parameters (e.g., permeability, elastic modulus) are employed directly, with microscale discontinuities (induced by temperature, external loads, or pore pressure) represented implicitly through the statistical evolution of these parameters.

(2) Darcy's law for fluid flow: Fluid motion under local pressure gradients obeys Darcy's law:

$$q = -\frac{k}{\mu}\nabla p, \tag{1}$$

where q is volumetric flux (m/s), k is permeability (m²), μ is dynamic viscosity (Pa·s), and ∇p denotes the hydraulic gradient.

(3) Negligible interfacial tension: Multiphase interfacial tension effects among water, steam, and kerogen pyrolysis products within fractures/pores are disregarded.

(4) Coupled hydrocarbon transport: Pyrolysis-derived hydrocarbons are assumed to migrate advectively with steam/condensate, with their independent transport behavior neglected due to trace concentrations.

(5) Instantaneous kerogen pyrolysis: Organic matter pyrolysis is considered complete upon reaching the threshold temperature, ignoring reaction kinetics and activation energy. This simplification is justified as the measured specific heat capacity of oil shale (which inherently includes kerogen) already incorporates the energy required for pyrolysis across temperature variations.

(6) Transversely isotropic porous media: The oil shale and its mudstone cap/base layers exhibit transverse isotropy in their poroelastic properties.

(7) Local thermal equilibrium: The timescale of heat exchange between pore fluids and the solid matrix is assumed negligible, permitting the use of a local thermal equilibrium equation for conductive–convective heat transfer.

2.2. THM coupling mathematical model

(1) Solid deformation equation

According to Salimzadeh et al. [23], the deformation field of saturated porous media satisfies the following differential equation:

$$\mathrm{div}(\mathbf{D}(\varepsilon-\varepsilon_{\mathrm{c}})-\alpha p\mathbf{I}-\beta_s\boldsymbol{K}(T-T_0)\mathbf{I})+\mathbf{F}=0, \tag{2}$$

where **D** is the stiffness matrix (see Table 1 for the meanings of all symbols used in Equations (2)–(10)). For anisotropic conditions, **D** is expressed as:

$$\mathrm{D}=\begin{bmatrix} C_{11} & C_{12} & C_{13} & 0 & 0 & 0 \\ C_{12} & C_{11} & C_{13} & 0 & 0 & 0 \\ C_{13} & C_{13} & C_{33} & 0 & 0 & 0 \\ 0 & 0 & 0 & C_{44} & 0 & 0 \\ 0 & 0 & 0 & 0 & C_{44} & 0 \\ 0 & 0 & 0 & 0 & 0 & \frac{C_{11}-C_{12}}{2} \end{bmatrix}, \tag{3}$$

where:

$$\begin{cases} C_{11}=E_{par}\left(E_{per}-E\nu_{per}^2\right)\Gamma \\ C_{33}=E_{per}\left(1-\nu_{par}^2\right)\Gamma \\ C_{12}=E_{par}(E_{per}\nu_{par}^2+E_{par}\nu_{per}^2)\Gamma \\ C_{13}=E_{par}E_{per}\nu_{par}\left(1+\nu_{par}\right)\Gamma \\ C_{44}=\mathrm{G}_{per} \\ C_{66}=\mathrm{G}_{par} \\ \Gamma=\frac{1}{(1+\nu_{par})\{(1-\nu_{par})E_{par}-2\nu_{per}^2E_{par}\}} \end{cases} \tag{4}$$

(2) Energy conservation equation

Based on Wang et al. [24], the heat transfer process during in situ thermal recovery of oil shale can be described by the following equations:

$$(\rho c_e)_{\mathrm{eff}}\frac{\partial T}{\partial t}+\rho_l c_{pl}\mathbf{q}\cdot\nabla T-\mathrm{div}(\boldsymbol{\lambda}_{\mathrm{eff}}\nabla T)=0, \tag{5}$$

$$(\rho c_e)=\phi\rho_l c_{pl}+(1-\phi)\rho_s c_{ps}, \tag{6}$$

$$\lambda_{\mathrm{eff}}=(1-\phi)\lambda_{\mathrm{s}}+\phi\lambda_{\mathrm{l}}. \tag{7}$$

The thermal conductivity tensor is given by:

$$\lambda_{\mathrm{s}}=\begin{bmatrix} \lambda_{\mathrm{s-par}} & 0 & 0 \\ 0 & \lambda_{\mathrm{s-par}} & 0 \\ 0 & 0 & \lambda_{\mathrm{s-per}} \end{bmatrix}. \tag{8}$$

(3) Mass conservation equation

According to Salimzadeh et al. [23], fluid flow in porous media satisfies the following mass conservation equation:

$$\mathrm{div}\left(\frac{\mathbf{k}}{\mu_l}(\nabla p + \rho_l g)\right) = \alpha\frac{\partial(\mathrm{div}\mathbf{u})}{\partial t} + C_p\frac{\partial p}{\partial t} - \phi\beta_T\frac{\partial T}{\partial t}. \tag{9}$$

The permeability tensor of oil shale is expressed as follows:

$$\mathbf{k} = \begin{bmatrix} k_{par} & 0 & 0 \\ 0 & k_{par} & 0 \\ 0 & 0 & k_{per} \end{bmatrix}. \tag{10}$$

Table 1. Meanings of symbols

Symbol	Meaning	Symbol	Meaning
D	Stiffness matrix	**I**	Second-order identity tensor
α	Biot coefficient	p	Fluid pressure
β_s	Thermal expansion coefficient of oil shale	T_0	Initial temperature of the domain
$\boldsymbol{K}$	Bulk modulus of oil shale matrix	$\boldsymbol{F}$	Body force component matrix
$\boldsymbol{E}_{par}$	Elastic modulus parallel to bedding plane	$\boldsymbol{E}_{per}$	Elastic modulus perpendicular to bedding plane
$\boldsymbol{v}_{par}$	Poisson's ratio parallel to bedding plane	$\boldsymbol{v}_{per}$	Poisson's ratio perpendicular to bedding plane
$\boldsymbol{\rho}_l$	Density of heated fluid	C_{pl}	Specific heat capacity of heated fluid
q	Velocity of heated fluid	$\boldsymbol{T}$	Temperature
$\boldsymbol{\rho}_s$	Density of oil shale	C_{ps}	Specific heat capacity of heated oil shale
$\boldsymbol{\lambda}_s$	Thermal conductivity tensor of oil shale	$\boldsymbol{\lambda}_l$	Thermal conductivity tensor of heated fluid
$\boldsymbol{\lambda}_{s-par}$	Thermal conductivity of oil shale parallel to bedding plane	$\boldsymbol{\lambda}_{s-per}$	Thermal conductivity of oil shale perpendicular to bedding plane
k	Permeability tensor of oil shale	μ_l	Dynamic viscosity of heated fluid
u	Deformation of oil shale	g	Gravitational acceleration
ϕ	Porosity of oil shale	$\boldsymbol{C}_p$	Compressibility coefficient of heated fluid

Continued on the next page

Table 1. *Continued*

Symbol	Meaning	Symbol	Meaning
β_T	Volumetric expansion coefficient of heated fluid	$\boldsymbol{k}_{par}$	Permeability of oil shale parallel to sedimentary bedding plane
$\boldsymbol{k}_{per}$	Permeability of oil shale perpendicular to sedimentary bedding plane	C_e	Equivalent specific heat capacity

As demonstrated by Wang et al. [25], oil shale exhibits significant permeability anisotropy. The permeability of oil shale in different directions under varying temperature conditions can be obtained through the following fitting equations:

$$k_{\mathrm{per}} = \begin{cases} 0 & (20 < T < 450\ ℃) \\ 2.46 \times 10^{-20}T + 1.081 \times 10^{-17} & (450 \le T < 550\ ℃) \\ -2.457 \times 10^{-21}T^2 + 2.805 \times 10^{-18}T + 7.868 \times 10^{-16} & (550 \le T \le 600\ ℃) \end{cases}, \quad (11)$$

$$k_{\mathrm{par}} = \begin{cases} -4.539 \times 10^{-22}T^2 + 2.036 \times 10^{-19}T - 5.419 \times 10^{-18} & (20 \le T < 350\ ℃) \\ 1.759 \times 10^{-20}T^2 - 1.212 \times 10^{-17}T + 2 \times 10^{-15} & (350 \le T \le 600\ ℃) \end{cases}. \quad (12)$$

The coupled THM mechanism of in situ thermal recovery of oil shale involves significant interactions among physical parameters. Based on extensive previous research, this study summarizes the theoretical and empirical formulas for key physical parameters in in situ thermal recovery of oil shale as functions of temperature, pore pressure, and time, as presented below:

$$\begin{cases} \rho_{\mathrm{g}} = 2272.7\frac{p \times 10^{-6}}{T+273} \\ \rho_{\mathrm{w}} = (0.9967 - 4.615 \times 10^{-5}T - 3.063 \times 10^{-6}T^2) \times 10^3 \\ \mu_{\mathrm{g}} = (0.36T + 88.37) \times 10^{-7} \\ \mu_{\mathrm{w}} = \left(\frac{1743-1.8T}{47.7T+759}\right) \times 10^{-3} \\ C_{\mathrm{g}} = -0.0001T^3 + 0.0948T^2 - 27.103T + 9246.8 \\ C_{\mathrm{w}} = 0.0165T^2 - 1.4878T + 4207.4 \\ \lambda_{\mathrm{g}} = 1.0 \times 10^{-8}T^3 - 4.0 \times 10^{-6}T^2 + 0.0006T + 0.0078 \\ \lambda_{\mathrm{w}} = -1.26 \times 10^{-5}T^2 + 2.56 \times 10^{-3}T + 0.5513 \\ \rho_{\mathrm{s}} = -8.0 \times 10^{-9}T^3 - 9.0 \times 10^{-6}T^2 + 0.0018T + 2.0919 \\ \phi = -5.0 \times 10^{-7}T^3 + 0.0005T^2 - 0.1028T + 7.2611 \\ \lambda_{s-per} = 1.176 \times 10^{-6}T^2 - 0.00285T + 1.9381 \\ \lambda_{s-par} = 4.563 \times 10^{-6}T^2 - 0.00119T + 0.7581 \end{cases}. \quad (13)$$

The aforementioned permeability fitting equations were derived from intact oil shale specimens and do not account for the enhanced heating effect caused by thermally induced fractures along bedding planes during steam injection. However, thermal fracturing in oil shale under steam stimulation primarily occurs along bedding planes, thereby improving permeability only in the parallel direction. Therefore, in this numerical simulation, the permeability perpendicular to bedding planes adopts the results from Wang et al. [25], while the permeability parallel to bedding planes is modified based on previous studies [26], as detailed below.

The permeability of oil shale parallel to bedding planes is primarily influenced by the density and aperture of interconnected fractures. At room temperature, oil shale is highly compact and intact, exhibiting extremely low permeability. However, at the meter scale, pre-existing fractures may exist due to diagenetic and geological processes, providing initial pathways for high-temperature steam during the early heating stage. Thus, it is assumed that the initial hydraulic fractures, propped by supporting agents, maintain high permeability (on the order of 10^{-12} to 10^{-1} m^2). The solid matrix is assumed to remain fracture-free below 350 °C, with its permeability determined by Wang et al. [25]. For newly formed interconnected fractures above 350 °C, permeability data from reference [27] are adopted. All permeability data are imported into the COMSOL Multiphysics software in the form of interpolation functions, as illustrated in Figure 1.

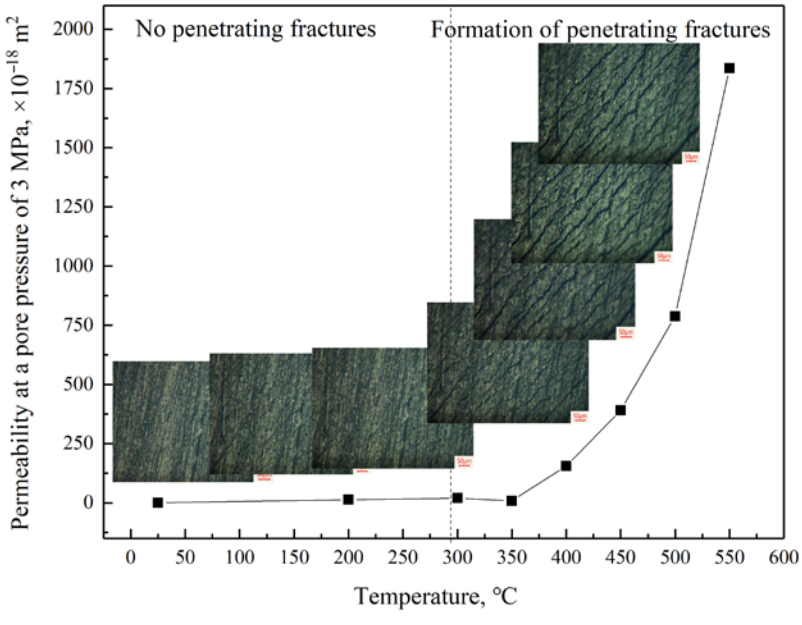

Fig. 1. Variation curve of oil shale permeability with temperature considering fracture evolution [27].

2.3. Establishment of the physical-geometric model

This study is primarily based on the occurrence conditions of oil shale in Barkol, Xinjiang, as the engineering background. Therefore, the physical-geometric model for numerical simulation is established according to the burial conditions of oil shale in Barkol. The average total thickness of the oil shale in Barkol is approximately 42.58 m, comprising about 22 oil shale layers with an average oil yield of 6.52%, while locally, the oil yield can exceed 10%. The burial depth of oil shale in this mining area ranges from the surface to 500 m underground, and the shallowly buried oil shale resources are currently being exploited via open-pit mining. The oil shale layers in this region exhibit a gentle occurrence, with a dip angle generally around 3°, though locally reaching up to 60°. The roof and floor strata of the oil shale layers are predominantly silty mudstone or mudstone, which are weakly aquiferous and act as aquicludes. The arid climate, absence of perennial surface water, and simple hydrogeological conditions in the mining area are favorable for the industrial practice of in situ steam injection for oil shale exploitation.

Based on the above considerations, the physical-geometric model for numerical simulation is simplified as follows:

(1) The dip angle of the oil shale layer is assumed to be 0°, i.e., a horizontal stratum.

(2) The depth from the surface to the top of the oil shale layer is 200 m, with a layer thickness of 40 m.

(3) The roof and floor strata are weakly aquiferous aquicludes with extremely low permeability, and no aquifers are present above or below the oil shale layer.

(4) A nine-well arrangement is adopted for the exploitation zone, consisting of one central steam injection well surrounded by eight production wells, as illustrated in Figure 2. The spacing between adjacent wells is 60 m. For numerical simulation, only a quarter of the model is considered, containing one injection well and three production wells located at the vertices of the model.

Research by Wang et al. [15] indicates that during in situ steam injection for oil shale exploitation, a fracture spacing of 20 m in the oil shale reservoir yields optimal heating efficiency and economic benefits. Given the assumed oil shale layer thickness of 40 m in this study, only cases with one and two hydraulic fractures are considered. For a single fracture, it is located at the mid-height of the oil shale layer. For two fractures, the upper fracture is 10 m below the roof, and the lower fracture is 10 m above the floor, with a vertical spacing of 20 m between them, both aligned along the bedding plane.

Furthermore, according to the findings in [27], when high-temperature steam is injected to heat oil shale, under a steam injection-to-production well spacing of 25 cm, the spacing of thermally induced fractures connecting the injection and production wells along the bedding plane is approximately 1 cm. Thus, it is assumed that the ratio of fracture spacing to well spacing under steam heating conditions is 1:25. Consequently, for a well spacing of 60 m,

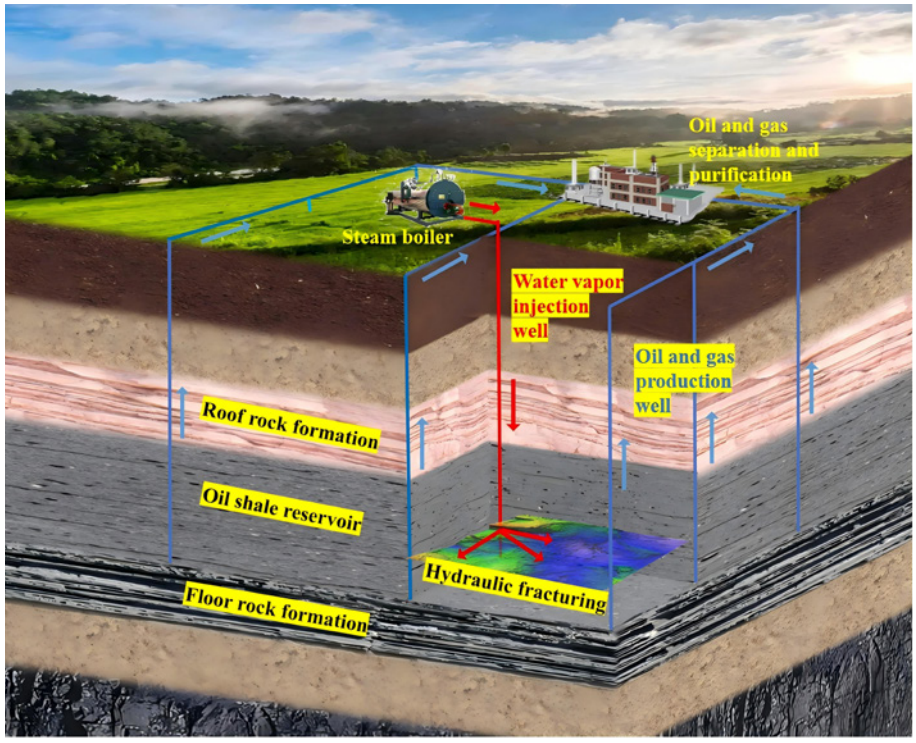

Fig. 2. Nine-well arrangement system for the in situ pyrolysis process of oil shale [27].

the spacing of thermally induced fractures should be 2.4 m. Therefore, this study assumes that weak planes are distributed every 2.5 m along the bedding plane in the oil shale layer. These weak planes remain closed at low temperatures (below 350 °C), exhibiting the same permeability as the solid matrix. When the temperature exceeds 350 °C, these weak planes evolve into interconnected fractures along the bedding plane. Once fractures form, they create new steam channels, allowing high-temperature steam to penetrate and further expand the heated zone. For comparison, cases without weak planes in the oil shale layer are also investigated. Table 2 summarizes the fracture and weak plane distributions for the four models studied.

The assumptions regarding weak plane spacing and extension distance in this study are extrapolated linearly from the results of [28]. The rationale for these assumptions is briefly explained as follows. Figure 3 shows oil shale core samples obtained via drilling in the Barkol oil shale mining area. Core analysis reveals abundant fractures and weak planes within the oil shale layers, with some intervals even containing large fracture zones. These fractures or weak planes are often associated with iron oxides, resulting in lower cementation strength. The cores obtained from drilling tend to break along these fractures or weak planes, which exhibit a wide range of scales, from micrometers to

meters. Figure 4 schematically illustrates the relationship between temperature field distribution and fracture development under steam heating. Initially, steam flows only along the initial fractures, heating the surrounding rock. Thermal fracturing of the heated rock generates new steam channels, further expanding the heating range. Thus, the assumptions regarding weak plane and fracture evolution in this study are reasonable.

It is important to note that the 2.5 m spacing is a conceptual model parameter derived from a linear extrapolation of laboratory-scale findings (1 cm fracture spacing under 25 cm well spacing [28]) to the field-scale well spacing of 60 m. While this provides a computationally tractable and mechanistically plausible representation of fracture network evolution, we acknowledge its inherent limitations. The actual spacing of natural weak planes and thermally induced fractures in a real reservoir is likely heterogeneous and influenced by in situ stress fields and geological discontinuities that are not fully captured in this model. Consequently, the absolute values of recovery and energy efficiency may be sensitive to variations in this assumed spacing. However, the primary conclusion of this study – that the activation of weak planes significantly enhances heating efficiency and recovery compared to models without them – is expected to hold qualitatively. Future work should include a systematic sensitivity analysis on this parameter once more field data becomes available to better constrain its range.

Table 2. Fracture distribution and weak surface distribution of different models

Model No.	Number of hydraulic fractures	Consideration of weak planes in the oil shale layer	Remarks
Model 1	1	No	The hydraulic fracture is located at the mid-depth of the oil shale layer, aligned along the bedding plane and connecting the injection and production wells.
Model 2	1	Yes	The hydraulic fracture is positioned at the mid-depth of the oil shale layer, following the bedding plane orientation and linking the injection and production wells. Weak planes are distributed every 2.5 m along the sedimentary bedding plane; these planes evolve into interconnected fractures between wells when the formation temperature exceeds 300 °C.
Model 3	2	No	The upper hydraulic fracture is 10 m below the roof of the oil shale layer, while the lower fracture is 10 m above the floor. These two fractures are spaced 20 m apart and both follow the bedding plane to connect the injection and production wells.
Model 4	2	Yes	The upper hydraulic fracture is 10 m below the roof, and the lower fracture is 10 m above the floor, with 20 m vertical spacing. Both fractures are bedding-aligned and connect the wells. Weak planes (spaced 2.5 m along bedding) thermally evolve into conductive fractures at temperatures > 300 °C.

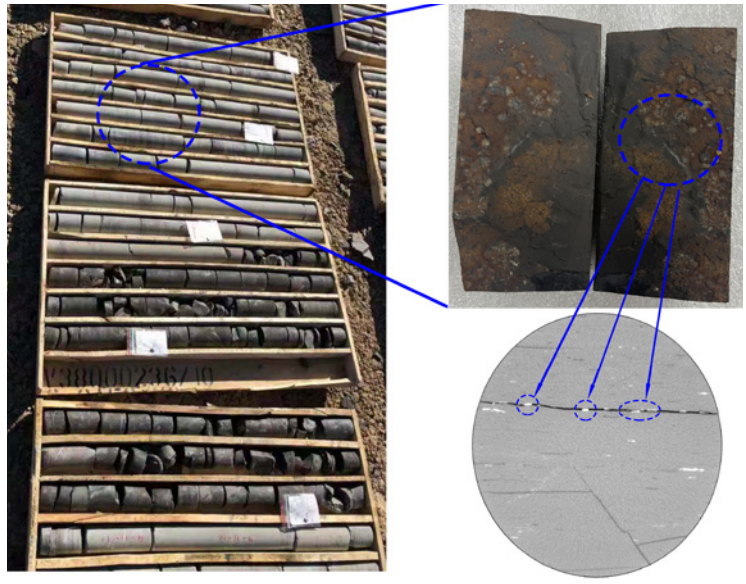

Fig. 3. Oil shale samples obtained by drilling.

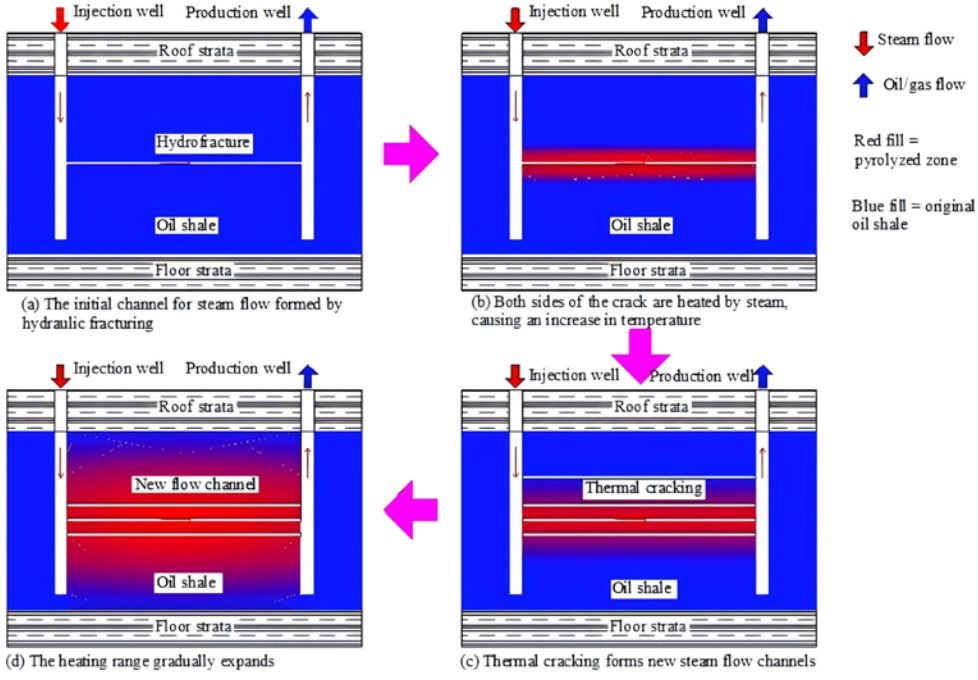

Fig. 4. Convection–conduction compound efficient heating mode for in situ exploitation of oil shale by superheated steam injection.

2.4. Determination of initial and boundary conditions for numerical simulation

Temperature field initial and boundary conditions: For numerical calculations in this study, the initial formation temperature is assumed to be 25 °C, while the temperature at the oil shale layer position in the injection well is set at 600 °C. The wellbore insulation is assumed to be effective, making all other boundaries free boundary conditions.

Solid deformation field initial and boundary conditions: The physical model's upper boundary is located 200 m below the surface. Therefore, a stress boundary condition of 5 MPa is applied to the top surface in the downward direction. The bottom (z = 0), left (y = 0), and back (x = 0) boundaries are fixed displacement boundaries with W = 0, V = 0, and U = 0, respectively, where U, V, and W represent displacements in the x, y, and z directions. Stress boundary conditions of 6 + γz MPa are applied to the surfaces where x and y equal 50 m, with directions as shown in Figure 5.

Seepage field initial and boundary conditions: The initial pore pressure in both the oil shale reservoir and cap rocks is assumed to be 0.1 MPa. The injection pressure at the oil shale layer section of the injection well is 3 MPa, while the production well pressure in the same section is 0.1 MPa.

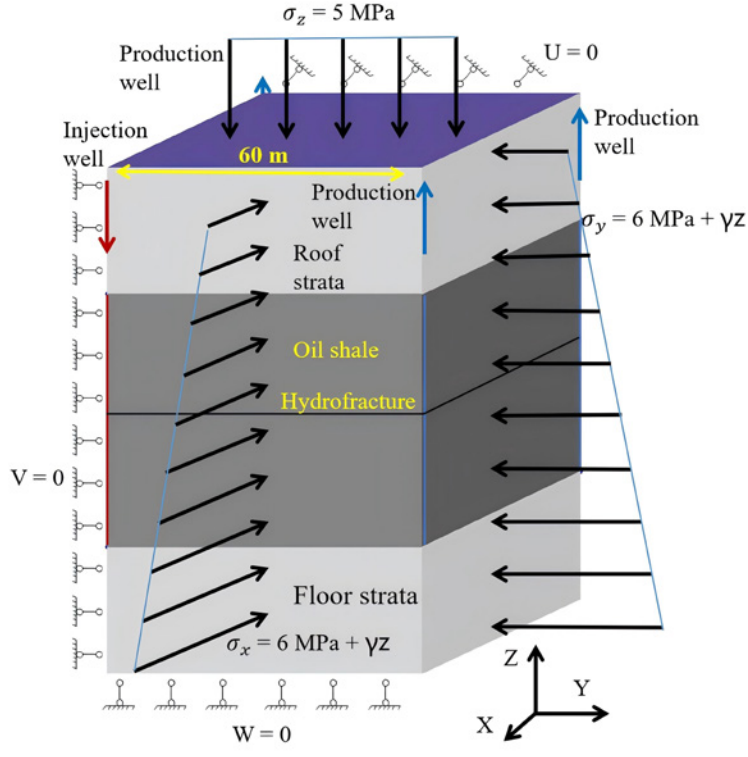

Fig. 5. Boundary conditions of numerical simulation (based on Model 1).

The wellbores are assumed to have excellent cementing conditions except in the oil shale layer section, meaning the internal fluid pressure has no effect on the surrounding rock's pore pressure.

Boundary conditions on symmetry planes: The numerical model utilizes a quarter-symmetry domain to simulate the full nine-well pattern, as shown in Figure 5. To accurately represent the symmetry of the full system, specific boundary conditions are applied to the symmetry planes (the planes at x = 0 and y = 0):

- Solid deformation field: These planes are defined as roller boundaries. This is implemented by constraining the normal displacement to zero; specifically, the displacement component U is set to zero on the symmetry plane at x = 0, and the displacement component V is set to zero on the symmetry plane at y = 0. This prevents motion across the symmetry planes while allowing for tangential deformation.
- Seepage field: The same symmetry planes are treated as impermeable (no-flux) boundaries. This condition ensures that no fluid flow occurs across these planes, which is physically consistent with the symmetry of the full well pattern, where these planes represent lines of symmetry in the flow field.

2.5. Calculation methods for recovery rate and energy return rate

According to the literature [29], the residual organic matter content in oil shale after heating by high-temperature steam at different temperatures shows good consistency with the thermogravimetric (TG) curve. Specifically, the residual organic matter content decreases with increasing temperature, and the temperature range of rapid organic matter reduction corresponds to the rapid mass loss range observed in TG experiments. CT observations reveal minimal residual organic matter above 550 °C, with no significant further reduction at higher temperatures. TG experiments also show markedly slower mass loss rates above 550 °C. Therefore, this study assumes that all mass loss in TG experiments represents conversion to oil/gas products, and temperatures above 550 °C indicate complete pyrolysis with 100% resource recovery. Based on these assumptions, the recovery rate (R_p) is calculated as follows:

$$R_P = \frac{\iiint_\Omega (1-\eta(T))\,\mathrm{d}\Omega}{\iiint_\Omega (1-\eta(550))\,\mathrm{d}\Omega}, \tag{14}$$

where $\eta(T)$ represents the oil shale TG curve. The mass loss is equated to oil/gas product mass, excluding effects from moisture evaporation. To minimize calculation errors, TG data from literature [29] are directly imported into COMSOL Multiphysics as interpolation functions (Fig. 6).

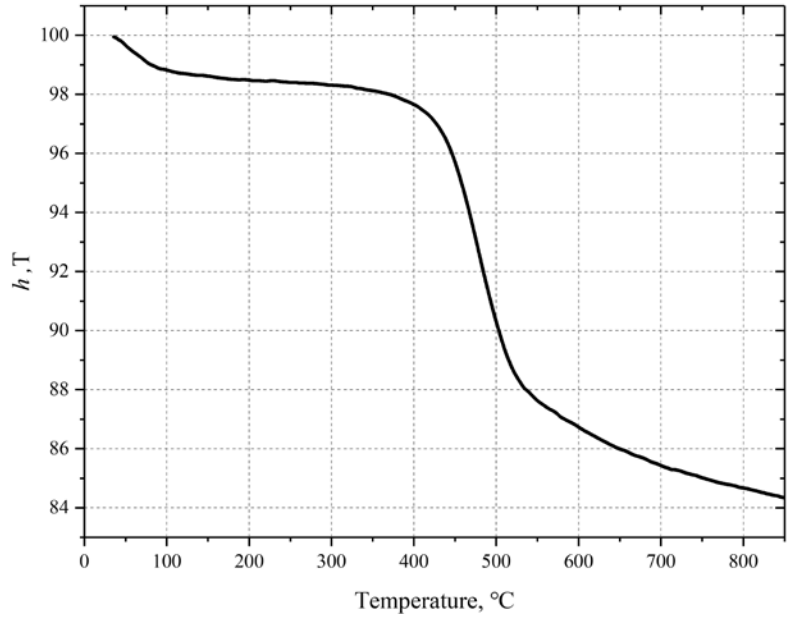

Fig. 6. Thermogravimetric curve of oil shale.

It is crucial to clarify the spatial context of the recovery calculation. The volume integrals in Equation (14) are computed over the entire quarter-symmetry numerical domain (Ω) established in Section 2.3 and illustrated in Figure 5. This domain contains one injection well and three production wells at its vertices, representing a symmetrical quarter of the full nine-well pattern. The recovery factor R_P thus calculated (e.g., the reported 90.5% for Model 4) represents the recovery efficiency achieved within this quarter-domain. The symmetric boundary conditions (zero normal displacement and zero fluid flux) applied at the symmetry planes (x = 0 and y = 0) ensure that the thermo-hydraulic-mechanical processes within this quarter-domain are representative of the processes occurring in the entire multi-well system. Therefore, the recovery factor from the quarter-domain is directly applicable to and representative of the performance of the full well pattern.

Previous numerical studies on in situ oil shale development primarily focused on the spatiotemporal evolution of temperature, seepage, and deformation fields, with some examining production characteristics. However, such limited focus provides inadequate guidance for industrial practice, which must consider economic viability. Without economic analysis, production-focused conclusions can be misleading. For energy development, the ERR serves as an effective economic indicator. This study therefore proposes key technical parameters based on R_E analysis.

The ERR is calculated as follows:

$$ERR = \frac{\text{Thermal energy of oil/gas products}}{\text{Injected thermal energy}}, \tag{15}$$

where the calorific value (E_p) of oil and gas products is calculated as 40 MJ/kg. This value is adopted as a representative weighted-average calorific value for the mixture of shale oil and pyrolysis gas generated from oil shale. The injected energy considers only the thermal energy carried by steam entering the oil shale layer through perforated pipes, excluding surface boiler and pipeline losses. The detailed formula is the following:

$$ERR = \frac{E_p \rho_s \iiint_{\Omega} (1-\eta(T))\mathrm{d}\Omega}{\int_0^t Q_g \rho_l(T) C_l(T)\mathrm{d}t}, \tag{16}$$

where Q_g is the steam injection rate (m^3/s), $\rho_l(T)$ is the high-temperature fluid density (kg/m^3) at temperature T, and $C_l(T)$ is the specific heat capacity ($J/(kg \cdot °C)$) of steam at temperature T.

3. Findings and discussion

3.1. Distribution and evolution of the reservoir temperature field during in situ steam injection for oil shale extraction

During in situ steam injection for oil shale extraction, the spatiotemporal distribution characteristics of temperature directly influence key parameters and technical indicators such as the permeability of the oil shale formation, oil recovery rate, and energy return rate. Table 3 presents the temperature field distribution of the oil shale formation for different models at various heating durations.

As shown in Table 3, during the initial heating stage, due to the extremely low permeability of the oil shale formation, a cylindrical high-temperature zone forms only near the steam injection well. Simultaneously, high-temperature steam flows through the initial fracture channels created by hydraulic fracturing, entering the interior of the oil shale formation and migrating toward the production well, forming a flattened high-temperature zone along the fracture paths. At one month of heating, the temperature field distributions of Models 1 and 2 are identical, while those of Models 3 and 4 are also nearly identical. This is because, in the early heating stage, high-temperature steam can only flow toward the production well through the initial hydraulic fractures. The surrounding rock adjacent to the fractures remains at a relatively low temperature, which is insufficient to induce the opening of weak planes in the oil shale formation to form interconnected steam channels between the injection and production wells.

As heating progresses, significant differences in temperature field distribution emerge among the models. Models 1 and 3 do not account for

the evolution of weak planes in the formation. Consequently, with prolonged heating, the high-temperature zone around the steam injection section expands annularly along the bedding planes of the oil shale, while the surrounding rock near the fractures continues to heat up via conduction. However, the expansion distance of the high-temperature zone remains limited due to the low thermal conductivity of oil shale, which hinders efficient large-scale heating through conduction alone. A comparison between Models 1 and 3 reveals that increasing the number of hydraulic fractures enhances heating efficiency, even without considering the influence of weak planes.

Table 3. Temperature distribution at different heating times

Time	Model 1	Model 2	Model 3	Model 4
30 d	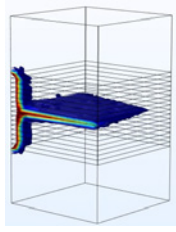	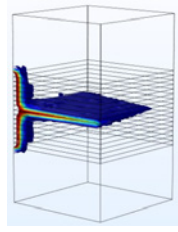	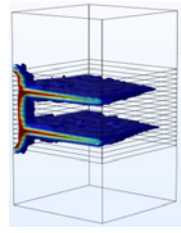	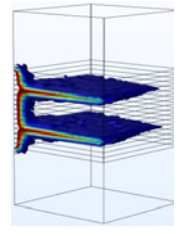
365 d	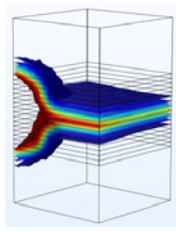	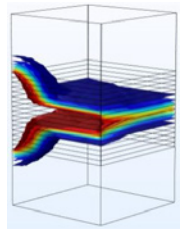	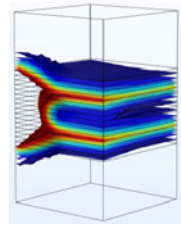	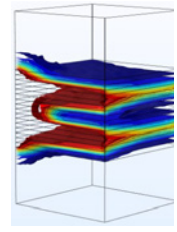
730 d	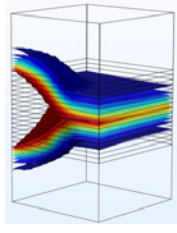	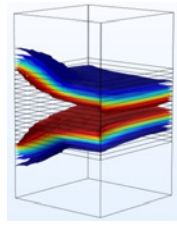	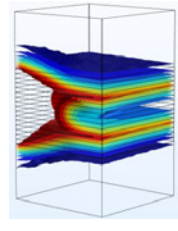	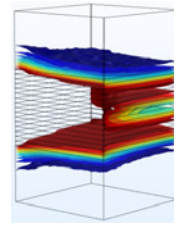
1000 d	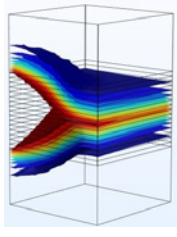	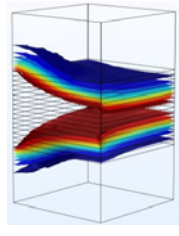	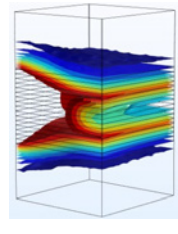	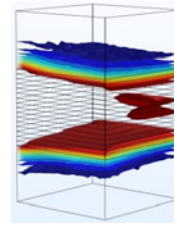

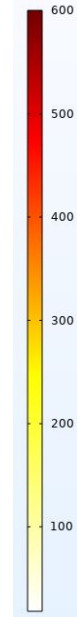

In contrast, Models 2 and 4 incorporate the influence of weak planes evolving into interconnected fractures on steam flow, resulting in fundamentally different temperature field distributions compared to Models 1 and 3. Under this condition, while high-temperature steam flows through the initial hydraulic fractures, the surrounding rock adjacent to the fractures is also heated. As the temperature of the surrounding rock rises and exceeds the thermal cracking threshold of oil shale (above 350 °C), fractures preferentially initiate along weak planes, forming bedding-parallel fractures. Once these newly formed fractures fully connect the injection and production wells, high-temperature steam enters the oil shale formation through these new pathways. At this stage, the heating mechanism transitions from conductive heating to convective steam heating along the newly formed fractures. Since convective heating is significantly faster than conduction, the temperature of the oil shale near the new fractures rises rapidly. Consequently, the flattened high-temperature zone expands perpendicular to the bedding planes. This alternating convection–conduction heating process facilitates rapid heating of the oil shale formation. A comparison between Models 2 and 4 demonstrates that increasing the number of hydraulic fractures accelerates heating.

Wang et al. [24] proposed constructing two 0.5 m-thick hydraulic fracture zones in the oil shale formation to serve as initial pathways for high-temperature steam. These zones exhibit high permeability, allowing steam to rapidly establish high-temperature regions and conductively heat the adjacent rock above and below. Simultaneously, as the temperature of the oil shale formation increases due to steam heating, the permeability of non-fractured regions improves, enabling steam to penetrate further and enhance heating. While this method achieves effective heating, creating thick fracture zones via hydraulic fracturing is challenging in practice. Unlike Wang's model, the proposed Models 3 and 4 feature two discrete fractures rather than thick zones, better reflecting real-world engineering conditions. Moreover, when accounting for weak plane evolution (Model 4), heating efficiency and oil recovery rates comparable to Wang's model can be achieved.

Figure 7 illustrates the temperature distribution in the oil shale formation at the production well (located 60 m from the injection well) under different heating durations. The results demonstrate significant variations in heating efficiency among the models despite identical well configurations, injection temperatures, and gas pressures.

Model 1 assumes only a single hydraulic fracture and no thermally activated weak planes that could evolve into interconnected fractures linking the injection and production wells. As shown in Figure 7(a), even after 2.5 years of heating, temperatures exceeding 600 °C were confined to the immediate vicinity of the hydraulic fracture. The surrounding rock exhibited a rapid thermal decline, dropping below 100 °C within 10 m of the fracture.

Model 2 incorporates the influence of weak planes evolving into permeable fracture networks. Figure 7(b) reveals that thermally activated weak planes significantly enhance heating efficiency, enabling a broad region of the oil

shale formation to reach pyrolysis temperatures. After 2.5 years, a 16-m-long high-temperature zone (> 500 °C) centered on the hydraulic fracture developed at the production well.

Model 3 disregards weak plane evolution but includes an additional hydraulic fracture. A comparison between Figure 7(a) and (c) indicates that dual fractures markedly expand the heated area. Initially, steam heats the rock adjacent to each fracture, with the inter-fracture zone gradually warming over time. By 2.5 years, the midpoint between the fractures reached 222 °C.

Model 4 combines dual fractures with weak plane activation. Figure 7(d) shows that early-stage heating was initially restricted to the fracture vicinity (258 °C at one month). However, after six months, the high-temperature zone expanded vertically, and by two years, the inter-fracture region homogenized at ~600 °C.

Notably, the transition from high-temperature (> 500 °C) to low-temperature (< 100 °C) zones remained within 20 m throughout the heating process. This phenomenon arises from the strong temperature dependence of oil shale permeability – high-temperature regions exhibit permeabilities 3–4 orders of magnitude greater than those of low-temperature zones. The resulting preferential steam flow into high-permeability areas further amplifies the thermal contrast. Low-permeability zones rely solely on conductive heating, which is inefficient due to oil shale's low thermal conductivity. This sharp thermal gradient forms a natural "thermal barrier" [30], minimizing heat loss and improving energy efficiency.

The "thermal barrier" is not a physical structure but a dynamic thermo-hydraulic phenomenon that arises from the coupling between localized convective heating within the fracture network and slow conductive heating of the intact oil shale matrix. Its formation can be attributed to three primary factors: (1) the inherently low thermal conductivity of oil shale, which restricts conductive heat spread; (2) the channelized flow of superheated steam, which creates a high-temperature zone bounded by the connected fracture pathways between injection and production wells; and (3) the sharp permeability contrast between this inner, fractured zone and the outer, intact rock mass, which prevents steam from penetrating beyond the active flow region. Consequently, the periphery of the heated zone relies solely on slow thermal conduction, resulting in a steep temperature decline that acts as an insulating layer. This mechanism is crucial for long-term energy efficiency, as it confines the injected thermal energy to the target production volume, thereby reducing parasitic heat loss to the surrounding formation and significantly enhancing the overall energy utilization ratio of the in situ conversion process.

However, once conductive heating raises low-temperature zones sufficiently to induce thermal fracturing, steam rapidly penetrates and heats these regions, converting them into high-permeability pathways. This dynamic process enables the progressive transformation of low-temperature zones into thermally productive areas.

(a) **Model 1**

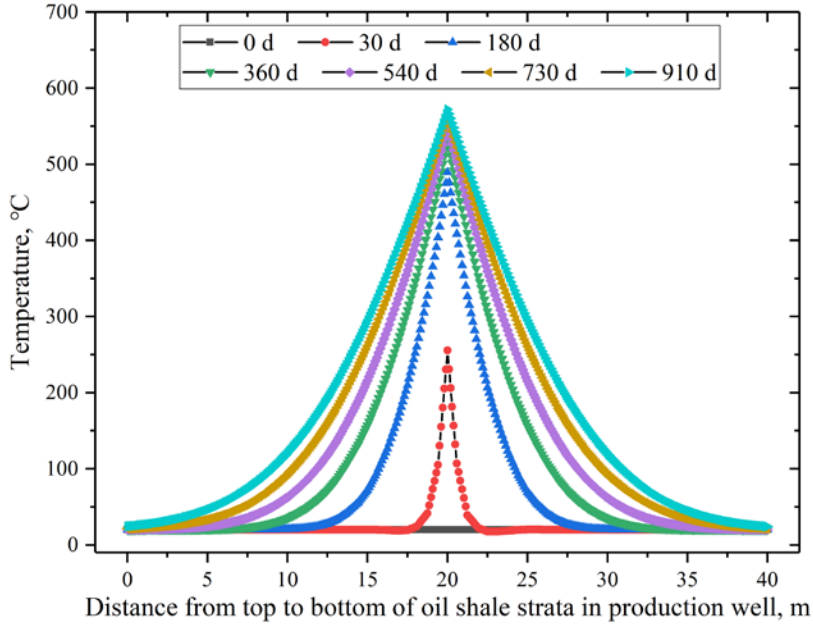

(b) **Model 2**

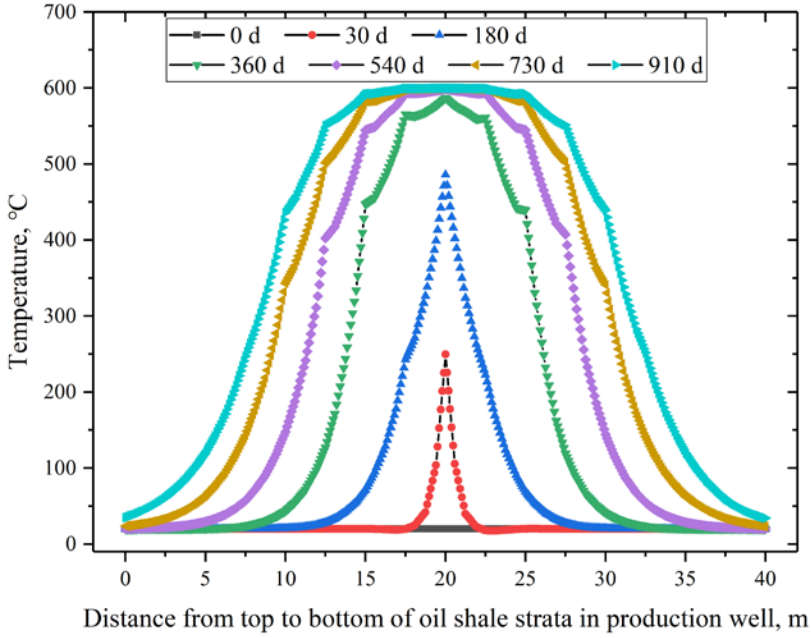

(c) **Model 3**

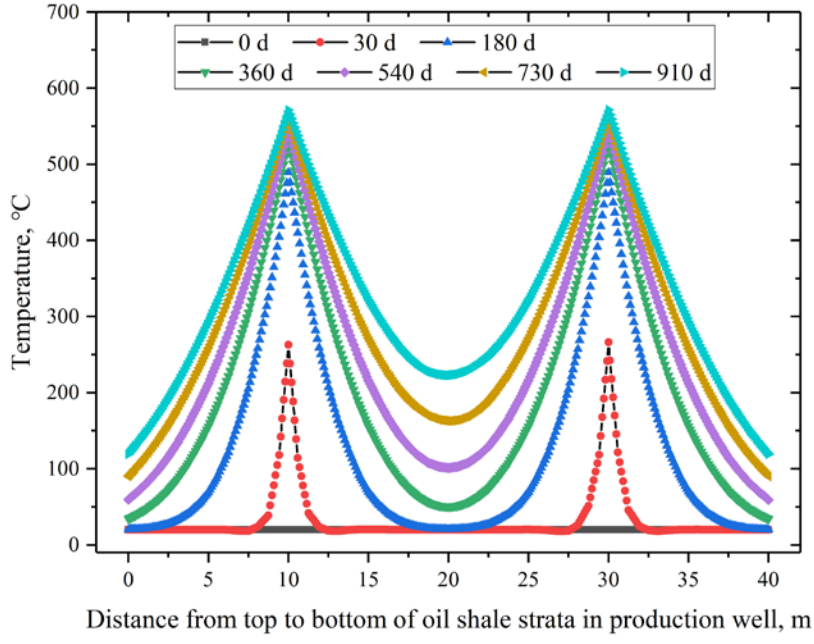

(d) **Model 4**

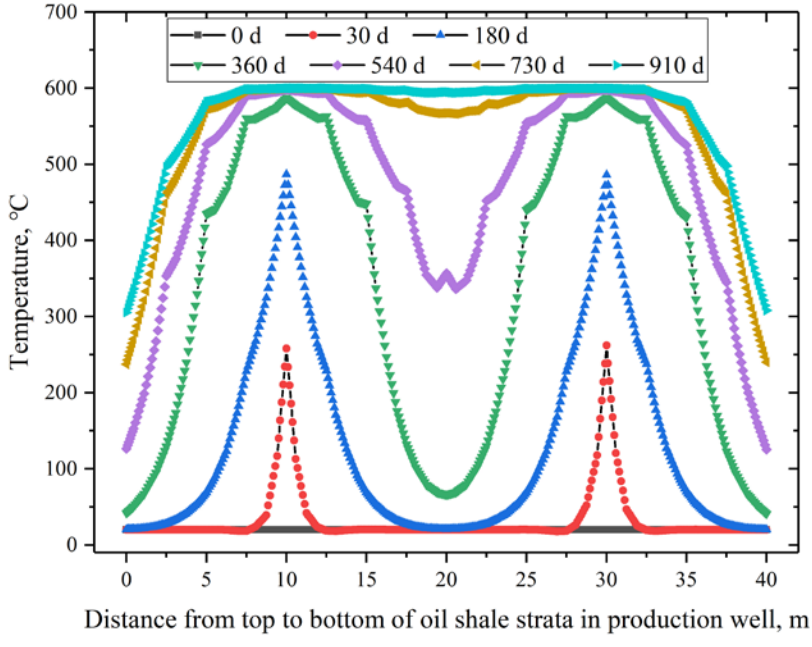

Fig. 7. Temperature distribution of the oil shale layer in the production well at different heating times.

3.2. Variation patterns of R_P and R_E with heating time

Hydrocarbon production and oil yield are critical process parameters for in situ thermal recovery of oil shale. Figure 8 illustrates the cumulative and daily hydrocarbon production curves of different models as a function of heating time. The results indicate that, under identical well patterns, well spacing, injection temperatures, and steam pressures, the hydrocarbon production trends of the models exhibit distinct characteristics.

Model 1 contains only a single hydraulic fracture and does not account for the influence of thermally induced weak-plane evolution into interconnected fractures on steam flow. As shown in Figure 8(a), during the initial heating stage, Model 1 achieves an average daily production of 36.92 t. This is attributed to the rapid heating of the oil shale adjacent to the fracture by high-temperature steam. However, as heating progresses, daily production declines sharply, dropping to 18.95 t by day 200 and further to below 14.6 t after 500 days. Cumulative production reaches 3053 t within the first 100 days, 10 054 t by day 500, and 16 231 t by day 1000, with a continuously decreasing growth rate. This phenomenon arises because the permeability of the rock surrounding the injection well increases due to thermal stimulation, creating a high-temperature zone. However, the absence of additional large-scale steam pathways restricts heat transfer primarily to conduction near the fracture, limiting the expansion of the heated region.

Model 3, which incorporates an additional hydraulic fracture, exhibits a similar trend but significantly higher production. The initial daily production reaches 59.3 t, declining to 28.57 t by day 200 and below 19.08 t after 500 days. By day 1000, cumulative production reaches 23 428 t, surpassing that of Model 1 in both daily and cumulative output.

Models 2 and 4 consider the evolution of weak planes into interconnected fractures under thermal stress, resulting in more complex production dynamics. Initially, the presence of hydraulic fractures leads to high daily production (33.10 t for Model 2 and 55.24 t for Model 4), which decreases by day 100 (19.47 t and 33.13 t, respectively) as pyrolysis near the initial fractures completes and new fracture networks develop. By day 200, thermally induced fractures form, allowing steam to penetrate deeper regions and temporarily boosting production. This cyclic process sustains relatively high production levels over extended periods, which is advantageous for industrial operations. However, after 600 days, production declines as a high-permeability thermal zone develops between wells, diverting steam flow and reducing the contribution of newly formed fractures.

(a) **Model 1**

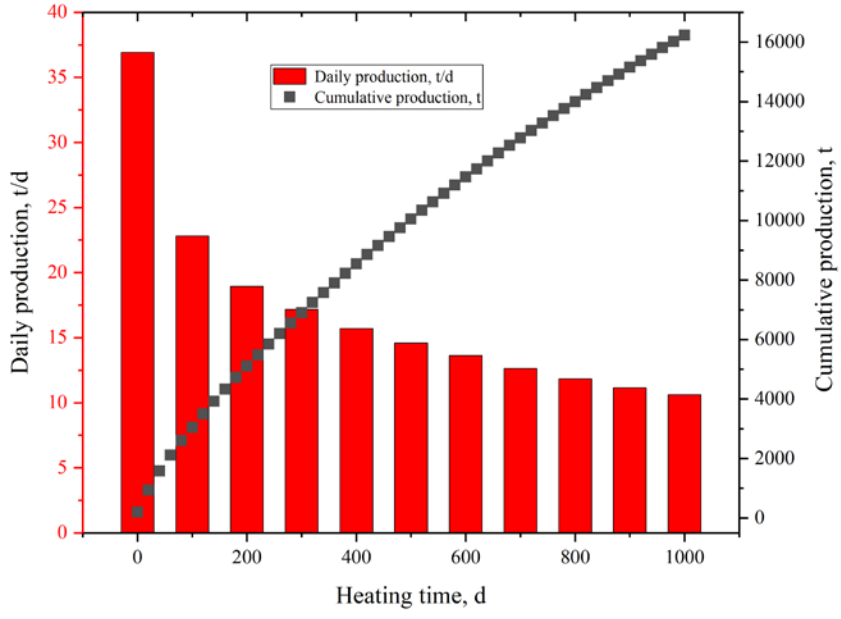

(b) **Model 2**

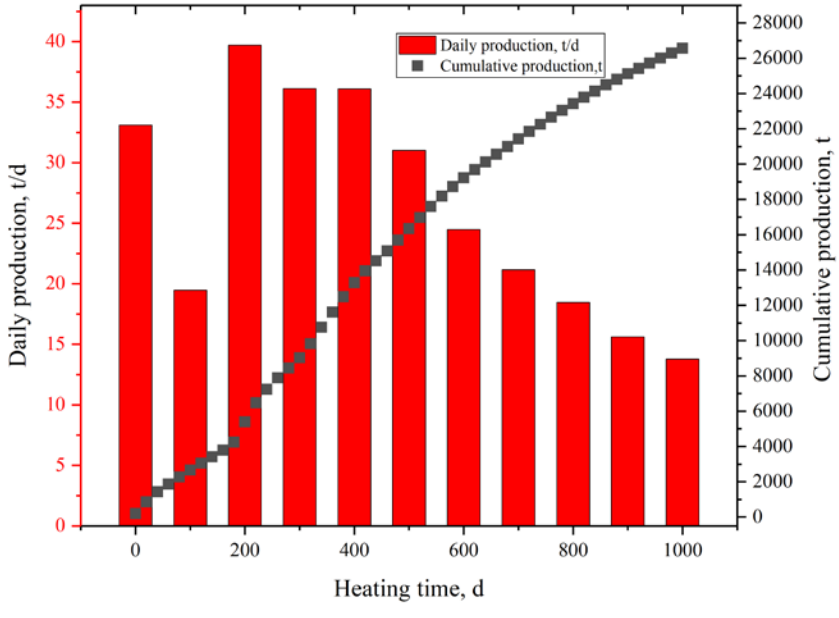

(c) **Model 3**

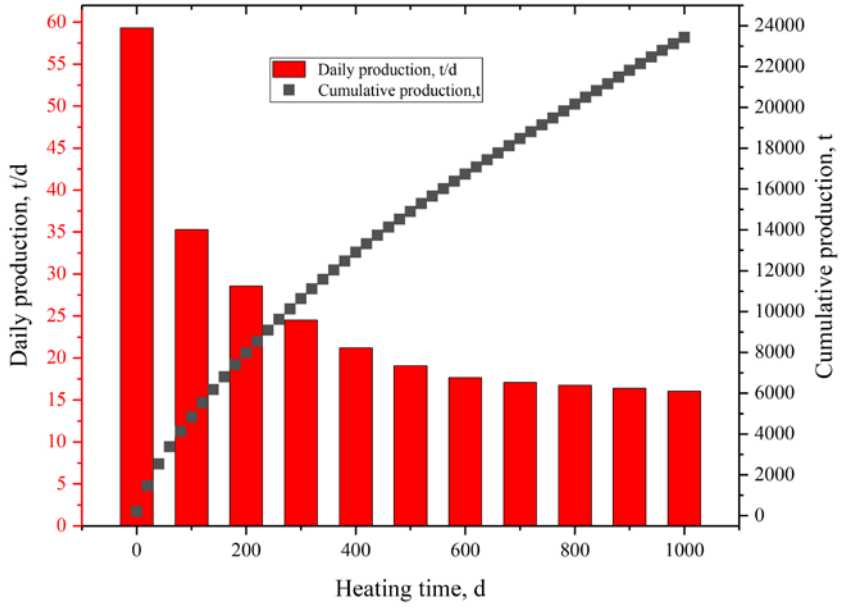

(d) **Model 4**

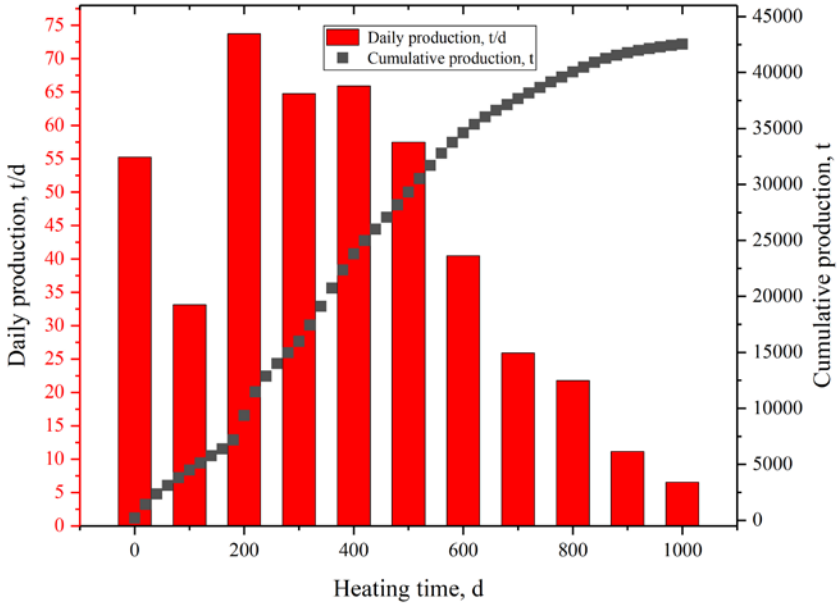

Fig. 8. Variation of oil shale oil and gas production with heating time.

Figure 9 presents the variation curves of oil yield with heating time for different models. As shown in Figure 9, when the heating duration is within 200 days, the differences in oil yield among the various models remain relatively small, all below 20%. However, when the heating time exceeds 200 days, significant discrepancies in oil yield begin to emerge.

For Model 1, the oil yield increases gradually with prolonged heating time, reaching only 34.5% after 100 days. The differences between Models 2 and 3 remain minimal throughout the heating process. Model 2 contains only one hydraulic fracture but accounts for the influence of thermally induced weak plane evolution into interconnected fractures on vapor flow, whereas Model 3 incorporates two hydraulic fractures without considering weak plane effects. The minor difference in oil yield between Models 2 and 3 indicates that both models achieve essentially identical volumes of pyrolyzed zones after heating.

In Model 2, the weak planes have not yet developed into interconnected fractures between the injection and production wells during the initial heating stage, while Model 3 benefits from two pre-existing hydraulic fractures serving as vapor flow channels. This configuration results in Model 3 exhibiting slightly higher oil yield than Model 2 during early heating stages. However, after 400 days of heating, Model 2 surpasses Model 1 in oil yield. Notably, none of Models 1, 2, or 3 achieve 60% oil yield even after 1000 days of heating, indicating suboptimal utilization of oil shale resources.

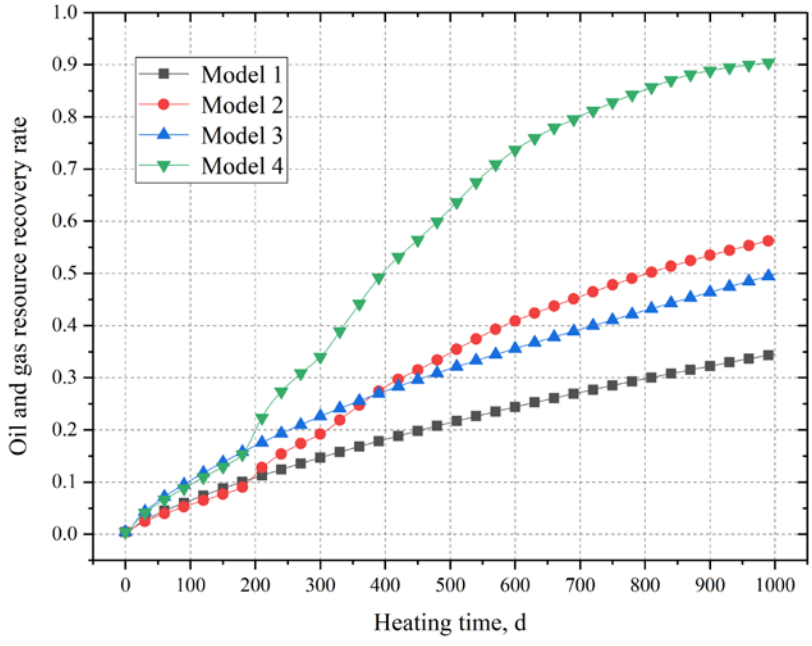

Fig. 9. Variation of oil yield by in situ steam injection with heating time.

In contrast, Model 4 maintains a high growth rate in oil yield during the first two years of heating, reaching 81.7% at the two-year mark and achieving 90.5% after 1000 days. The substantial improvement in oil yield achieved by Model 4 (which differs from Model 2 only by one additional hydraulic fracture) demonstrates that appropriately increasing the number of initial fracture channels through staged fracturing can significantly enhance both oil/gas production and recovery efficiency during in situ oil shale thermal recovery operations.

3.3. Temporal variation of energy return rate in in situ steam injection for oil shale recovery

For the industrial-scale exploitation of oil shale, if a particular in situ extraction method fails to achieve favorable economic benefits, large-scale industrial application becomes unfeasible. This study employs the ERR as an indicator to evaluate the economic viability of in situ steam injection for oil shale recovery. Figure 10 illustrates the variation of the ERR with heating time under four different models.

As shown in Figure 10, when steam is used as the heat-carrying medium, a high ERR can be achieved in the early stages of heating, whereas Shell's electrical heating technology requires a prolonged preheating period before oil production begins. This indicates that steam heating technology can deliver economic benefits at an earlier stage.

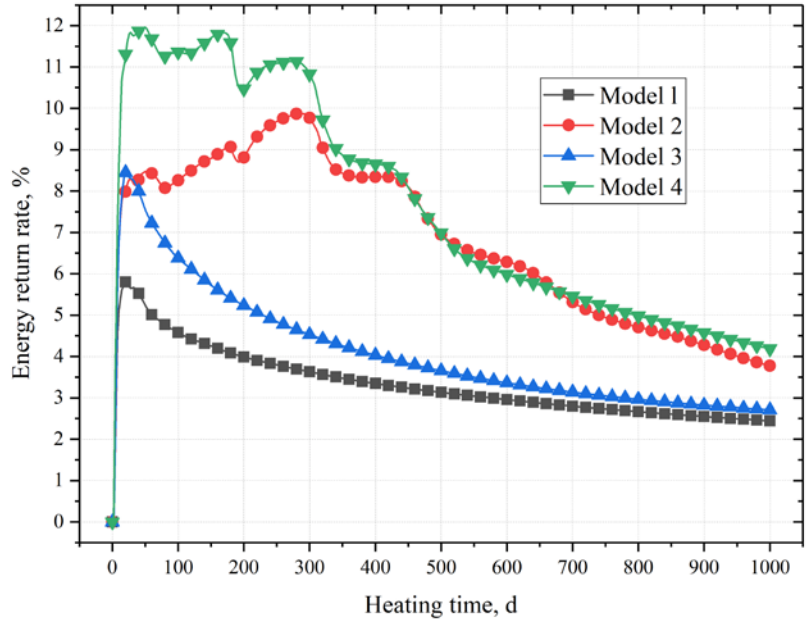

Fig. 10. Energy return rate of in situ steam injection for oil shale recovery as a function of heating time.

The ERR trends vary significantly among the different models. Models 1 and 3 do not account for the influence of thermally induced weak planes evolving into interconnected fractures on steam flow. In these models, the ERR peaks shortly after heating begins, reaching 5.79 and 8.44, respectively. However, as heating continues, the ERR gradually declines. This is because, in the initial phase, the pre-existing hydraulic fractures provide pathways for steam flow, allowing rapid heating and pyrolysis of oil shale near the fractures, thereby enhancing hydrocarbon production. Over time, the oil shale adjacent to the fractures is fully pyrolyzed, while regions farther away lack efficient steam channels, relying solely on slow thermal conduction. Consequently, hydrocarbon production decreases, leading to a continuous decline in the ERR.

Although Model 3 incorporates an additional hydraulic fracture compared to Model 1, its peak ERR is only 1.46 times that of Model 1. This is because, under identical well configurations, injection temperatures, and steam pressures, increasing the number of fractures also raises steam flow rates (as shown in Figure 11), thereby increasing energy input. As a result, the ERR does not improve proportionally with the number of fractures.

Models 2 and 4 consider the evolution of weak planes into interconnected fractures under thermal effects, with the only difference being that Model 2 has one hydraulic fracture while Model 4 has two. The ERR trends for these two models exhibit high similarity. Within the first year of heating,

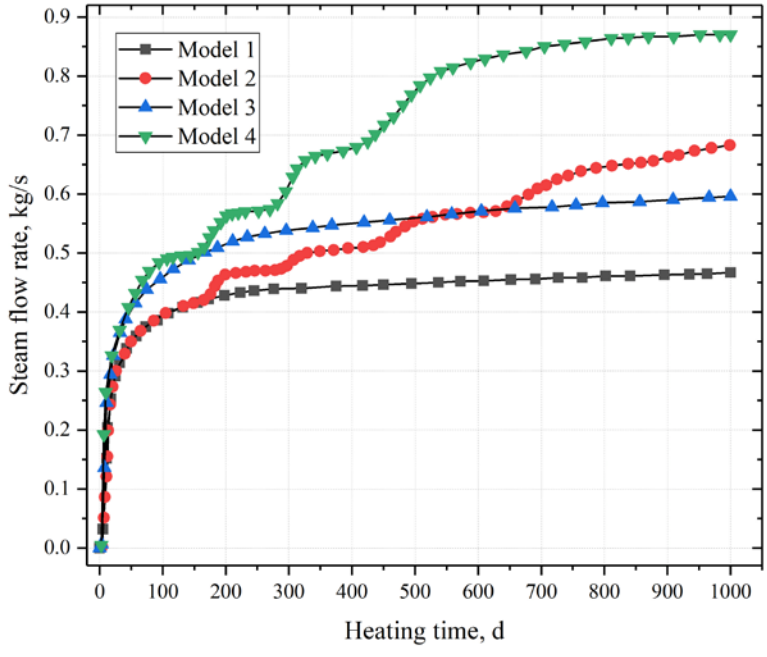

Fig. 11. Variation of steam flow rate as a function of heating time.

the ERR fluctuates significantly. These fluctuations occur because newly formed fractures connecting the injection and production wells allow high-temperature steam to rapidly penetrate and heat adjacent oil shale, leading to transient increases in the ERR as pyrolysis occurs. This cyclic process results in oscillatory behavior in the ERR. After one year, the ERR for both models begins to decline steadily without further fluctuations.

Considering the construction, operation, and maintenance costs of the entire extraction system, this study defines an ERR threshold of 5 for economically viable production. Models 1, 2, 3, and 4 fall below this threshold after 60, 740, 228, and 794 days of heating, respectively. The addition of a second fracture in Model 3 extends the viable production period by 168 days compared to Model 1, demonstrating that increasing fracture density can prolong production when thermal fracture evolution is negligible. However, Model 4 shows only marginal improvement over Model 2, indicating that when thermally activated fractures dominate flow pathways, the influence of additional hydraulic fractures on the ERR becomes negligible. Nevertheless, as seen in Figure 9, the number of fractures significantly impacts oil recovery efficiency.

4. Conclusions

This study investigates the spatiotemporal evolution of temperature fields during in situ steam injection for oil shale exploitation based on an anisotropic THM (thermo-hydro-mechanical) coupled mathematical model, while analyzing the variations in oil/gas production, oil recovery rate, and energy return rate with heating duration. The key findings are summarized as follows:

1. The evolution of thermally activated fractures from pre-existing weak planes plays a pivotal role in enhancing heating efficiency during in situ steam injection. These fractures facilitate alternating convection–conduction heating modes, enabling vertical expansion of high-temperature zones and achieving 90.5% oil recovery after 1000 days. In contrast, models relying solely on initial hydraulic fractures exhibit limited heating (< 60% recovery) due to restricted steam pathways.
2. Daily oil/gas production declines rapidly in models without fracture evolution (e.g., from 36.92 t/d to 14.6 t/d in Model 1), whereas models incorporating weak plane activation sustain higher yields by forming new steam flow channels. Notably, doubling hydraulic fractures (Model 3 vs. Model 1) improves cumulative production by 44%, highlighting the importance of initial fracture design.
3. Energy return rates (ERR) demonstrate divergent trends: models excluding fracture evolution exhibit early peaks (ERR = 5.79–8.44) followed by exponential decay, while models with weak plane activation maintain ERR > 5 for over a year. However, doubling hydraulic fractures only

marginally increases peak ERR (1.46×), emphasizing the trade-off between steam input and recovery gains.

4. Field applications should prioritize hydraulic fracturing to create interconnected fracture networks while leveraging natural weak planes to maximize convective heating. This dual strategy optimizes both technical performance (recovery > 90%) and economic viability (sustained ERR), offering a scalable solution for deep oil shale exploitation.

Data availability statement

The datasets generated and/or analyzed during this study are available from the corresponding author upon reasonable request.

Acknowledgments

This study was supported by the Open Fund of the State Center for Research and Development of Oil Shale Exploitation, the Basic Research Program of Shanxi Province (grant No. 20210302123177), and the National Key Research and Development Program of China (grant No. 2019YFA0705501). We acknowledge the use of Deep Seek for language editing and proofreading of this manuscript. AI assistance was used to improve grammar, clarity, and readability. All intellectual contributions, data interpretation, and conclusions remain the sole responsibility of the authors. The publication costs of this article were partially covered by the Estonian Academy of Sciences.

References

1. Guo, W., Pan, J., Yang, Q., Li, Q., Deng, S., Zhu, C. Study of the residual carbon oxidation trigger mechanism in fractured oil shale formation under real condition. *International Communications of Heat and Mass Transfer*, 2025, **160**, 108369. https://doi.org/10.1016/j.icheatmasstransfer.2024.108369
2. Yang, D., Wang, L., Zhao, Y., Kang, Z. Investigating pilot test of oil shale pyrolysis and oil and gas upgrading by water vapor injection. *Journal of Petroleum Science and Engineering*, 2021, **196**, 108101. https://doi.org/10.1016/j.petrol.2020.108101
3. Lei, Z., Zhang, Y., Yang, Z., Shi, Y., Zhang, H., Li, X. et al. Numerical simulation of oil shale in-situ exploration productivity comparison between steam injection and electrical heating. *Applied Thermal Engineering*, 2024, **238**, 121928. https://doi.org/10.1016/j.applthermaleng.2023.121928
4. Kang, Z., Zhao, Y., Yang, D. Review of oil shale in-situ conversion technology. *Applied Energy*, 2020, **269**, 115121. https://doi.org/10.1016/j.apenergy.2020.115121

5. Saif, T., Lin, Q., Gao, Y., Al-Khulaifi, Y., Marone, F., Hollis, D. et al. 4D *in situ* synchrotron X-ray tomographic microscopy and laser-based heating study of oil shale pyrolysis. *Applied Energy*, 2019, **235**, 1468–1475. https://doi.org/10.1016/j.apenergy.2018.11.044
6. Zhang, Y., Zhao, X., Wang, Q., Che, Y., Liu, H., Mu, R. et al. A study on the structures and primary reaction products of kerogens in Longkou oil shale with different densities through supercritical ethanolysis. *Journal of Molecular Structure*, 2024, **1309**, 138151. https://doi.org/10.1016/j.molstruc.2024.138151
7. Kibodeaux, K. R. Evolution of porosity, permeability, and fluid saturations during thermal conversion of oil shale. In *SPE Annual Technical Conference and Exhibition*, October 27–29, 2014, Amsterdam, The Netherlands. https://doi.org/10.2118/170733-ms
8. Xiao, H., Hu, T., Pang, X., Ding, C., Xu, Y., Zhang, S. et al. A novel method for identifying oil content and moveable thresholds in heterogeneous shales. *Fuel*, 2025, **397**, 135473. https://doi.org/10.1016/j.fuel.2025.135473
9. Li, Q., Wei, H., Zhang, Y., Han, L., Han, S., Ding, N. The variations on thermal conductivity and structures of silty clay modified by waste fly ash and oil shale ash after freeze–thaw cycles. *Construction and Building Materials*, 2020, **260**, 119954. https://doi.org/10.1016/j.conbuildmat.2020.119954
10. Wang, G., Yang, D., Liu, S., Fu, M., Wang, L. Experimental study on the anisotropic mechanical properties of oil shales under real-time high-temperature conditions. *Rock Mechanics and Rock Engineering*, 2021, **54**, 6565–6583. https://doi.org/10.1007/s00603-021-02624-7
11. Baqain, M., Neshumayev, D., Konist, A. TG-MS analysis and kinetic study of co-combustion of ca-rich oil shale with biomass in air and oxy-like conditions. *Carbon Capture Science & Technology*, 2024, **10**, 100162. https://doi.org/10.1016/j.ccst.2023.100162
12. Huang, H. W., Yu, H., Xu, W. L., Lyu, C. S., Micheal, M., Xu, H. Y. et al. A coupled thermo-hydro-mechanical-chemical model for production performance of oil shale reservoirs during in-situ conversion process. *Energy*, 2023, **268**, 126700. https://doi.org/10.1016/j.energy.2023.126700
13. Liu, Y., Xue, L., Ma, J., Peng, C., Bai, F., Li, Y. et al. Three-dimensional numerical simulation, energy efficiency and economic benefit estimation of oil shale in situ pyrolysis process. *Geoenergy Science and Engineering*, 2023, **227**, 211804. https://doi.org/10.1016/j.geoen.2023.211804
14. Kang, Z., Xie, H., Zhao, Y., Zhao, J. The feasibility of in-situ steam injection technology for oil shale underground retorting. *Oil Shale*, 2020, **37**(2), 119–139. https://doi.org/10.3176/oil.2020.2.03
15. Wang, G., Liu, S., Yang, D., Fu, M. Numerical study on the in-situ pyrolysis process of steeply dipping oil shale deposits by injecting superheated water steam: a case study on Jimsar oil shale in Xinjiang, China. *Energy*, 2022, **239**, 122182. https://doi.org/10.1016/j.energy.2021.122182
16. Zhang, Z., Montilla, M. J. B., Xie, Z., Li, S., Hu, Y., Li, X. Comparative analysis of wellbore electrical heating, low-frequency heating, and steam injection for

in-situ conversion in continental shale oil reservoirs. *Case Studies in Thermal Engineering*, 2024, **64**, 105512. https://doi.org/10.1016/j.csite.2024.105512

17. Zhu, J., Yi, L., Yang, Z., Li, X. Numerical simulation on the in situ upgrading of oil shale reservoir under microwave heating. *Fuel*, 2021, **287**, 119553. https://doi.org/10.1016/j.fuel.2020.119553
18. Zhu, J., Yi, L., Yang, Z., Duan, M. Three-dimensional numerical simulation on the thermal response of oil shale subjected to microwave heating. *Chemical Engineering Journal*, 2021, **407**, 127197. https://doi.org/10.1016/j.cej.2020.127197
19. Lou, X., Wang, J., Liu, H. Numerical simulation on in-situ modification of oil shale electric heating based on off-grid photovoltaic power supply. *Renewable Energy*, 2025, **242**, 122511. https://doi.org/10.1016/j.renene.2025.122511
20. Tian, W., Xu, R., Zeng, K., Chen, J., Yu, R., Jiang, P. Energy evolution during in-situ conversion of low-maturity shales. *Energy*, 2025, **317**, 134593. https://doi.org/10.1016/j.energy.2025.134593
21. Zheng, S., Liu, B., Mohammadian, E., Liu, Y., Tian, S. Sustainable in-situ steam injection approach for shale oil extraction in Xinjiang, China: a technical and economic analysis. *Energy*, 2024, **308**, 132986. https://doi.org/10.1016/j.energy.2024.132986
22. Zhang, Z., Montilla, M. J. B., Li, S., Xu, T., Li, Y., Xie, Z. et al. Evaluating heating strategies for efficient in-situ shale oil conversion: a numerical approach using THC coupled modeling. *Applied Thermal Engineerin*g, 2025, **270**, 126203. https://doi.org/10.1016/j.applthermaleng.2025.126203
23. Salimzadeh, S., Paluszny, A., Nick, H. M., Zimmerman, R. W. A three-dimensional coupled thermo-hydro-mechanical model for deformable fractured geothermal systems. *Geothermics*, 2018, **71**, 212–224. https://doi.org/10.1016/j.geothermics.2017.09.012
24. Wang, G., Yang, D., Kang, Z., Zhao, J., Lv, Y. Numerical investigation of the in situ oil shale pyrolysis process by superheated steam considering the anisotropy of the thermal, hydraulic, and mechanical characteristics of oil shale. *Energy & Fuels*, 2019, **33**(12), 12236–12250. https://doi.org/10.1021/acs.energyfuels.9b02883
25. Wang, G., Yang, D., Zhao, Y., Kang, Z., Zhao, J., Huang, X. Experimental investigation on anisotropic permeability and its relationship with anisotropic thermal cracking of oil shale under high temperature and triaxial stress. *Applied Thermal Engineering*, 2019, **146**, 718–725. https://doi.org/10.1016/j.applthermaleng.2018.10.005
26. Zhang, Y., Wang, L., Yang, D., Kang, Z., Zhao, J., Huang, X. et al. CT imaging to study meso-structure evolution of fractured oil shale during in-situ pyrolysis by high-temperature water vapor injection. *Geoenergy Science and Engineering*, 2024, **241**, 213104. https://doi.org/10.1016/j.geoen.2024.213104
27. Huang, X., Kang, Z., Zhao, J., Wang, G., Zhang, H., Yang, D. Experimental investigation on micro-fracture evolution and fracture permeability of oil shale heated by water vapor. *Energy*, 2023, **277**, 127677. https://doi.org/10.1016/j.energy.2023.127677

28. Huang, X., Yang, D., Wang, G., Zhang, K., Zhao, J. Evolution patterns and anisotropic connectivity characteristics of pores and fissures in oil shale after steam heating at different temperatures. *Natural Resources Researc*h, 2024, **34**, 409–425. https://doi.org/10.1007/s11053-024-10406-5
29. Huang, X., Yang, D., Kang, Z. Three-phase segmentation method for organic matter recognition in source rocks via CT images: a case study on oil shale pyrolyzed by steam. *Energy & Fuels*, 2021, **35**(12), 10075–10085. https://doi.org/10.1021/acs.energyfuels.1c00917
30. Yang, D., Zhao, Y., Kang, Z. Numerical simulation of in situ exploitation of oil shale by injecting high-temperature steam. *Oil Shale*, 2019, **36**(4), 483–500. https://doi.org/10.3176/oil.2019.4.03